Common-Reflection-Surface Stack

Jürgen Mann, Steffen Bergler, and Peter Hubral, Geophysical Institute, University of Karlsruhe, Germany*

Summary

The Common-Reflection-Surface (CRS) Stack was originally introduced as a data-driven method to simulate zero-offset sections from 2-D seismic reflection pre-stack data. The noteworthy results received for various synthetic and real data examples encouraged us to transfer the approach to more general problems, namely the simulation of finite-offset sections for 2-D pre-stack data as well as the simulation of zero-offset volumes for 3-D data. In the first part of this contribution, we focus on these generalizations of the Common-Reflection-Surface Stack and briefly indicate implementation strategies for the zero-offset simulation in 3-D and the finite-offset simulation in 2-D. Furthermore, we discuss several applications of the kinematic CRS wavefield attributes. They are, e. g., suited for true amplitude analysis, inversion, and parsimonious migration. In addition to this basic discussion of the CRS method, practical examples will be given in the talk.

Introduction

The Common-Reflection-Surface (CRS) Stack was introduced by Müller (1998) and Müller et al. (1998) as a data-driven zero-offset (ZO) simulation method for 2-D that does not require an explicit knowledge of the macro velocity model. The CRS stack assumes the subsurface to be set up by reflector segments with arbitrary location, orientation, and curvature. The CRS stacking operator approximates the kinematic reflection response of such a reflector segment. In contrast, the operators of, e. g., Kirchhoff migration or normal moveout/dip moveout/stack are defined as the responses of diffractors or ZO isochron segments in the subsurface, respectively. Obviously, the latter two approaches represent special cases of the CRS stack approach: on the one hand, a diffraction point can be described as a reflector segment with infinite curvature, on the other hand, the curvature of a reflector segment could also coincide with the curvature of a ZO isochron segment.

A model-based application of the CRS stack is hardly applicable as it requires a detailed description of the model including all interfaces—a smooth macro velocity model is not sufficient for this task. However, in the scope of paraxial zero-order ray theory, the three properties of the reflector segment are associated with a set of wavefield attributes that represent propagation directions and curvatures of certain hypothetical wavefronts. With these wavefield attributes, an analytic approximation of the kinematic reflection response of the reflector segment can be derived. This approximate response, in the following also called CRS stacking operator, and its associated wavefield attributes can be directly determined from the pre-stack data by means of coherence analysis. In other words, the optimum CRS stacking operator for a particular ZO sample to be simulated can be determined in a data-driven way without the need to know the actual location, orientation, and curvature of the corresponding reflector segment. Thus, the CRS stack approach implies a generalization of the well-known CMP stack and velocity analysis. However, instead of only one wavefield attribute, the stacking velocity,[1] the CRS stack provides an entire set of wavefield attributes that parameterize the subsurface model and serve for various applications: e. g., the geometrical spreading factor and the projected Fresnel zone can be estimated, or diffraction and reflection events can be separated by means of the attributes.

Applications of the CRS stack for the simulation of 2-D ZO sections can be found in Mann et al. (1999) and Jäger et al. (2001). Further improvements of the "classic" CRS stack for 2-D, namely the handling of conflicting dip situations, were introduced by Mann (2001).

3-D zero-offset simulation

For the ZO case, the reflector segment's properties and the associated wavefield attributes are related to each other by two hypothetical experiments. For ZO, we assume only unconverted primary events with normal incidence on the reflecting interface. In this case, the up-going and down-going ray branches coincide. The up-going ray branch is called the normal ray in the following. For the first experiment, a point source is placed at the normal incidence point (NIP) of the normal ray on the reflector segment. The wavefront emanating from this experiment, the so-called NIP wave, propagates along the normal ray and emerges at the acquisition surface with well-defined curvature and propagation direction. In the second experiment, a simultaneous excitation of the entire reflector segment (exploding reflector experiment) is performed to obtain the so-called normal wave. Again, the wavefront propagates along the normal ray and emerges with a certain curvature and the same propagation direction as in the first experiment.

For the 2-D case, both curvatures as well as the propagation direction can be expressed as scalars. Thus, we receive three wavefield attributes for this simplest case. The 2-D ZO case was thoroughly discussed by Mann et al. (1999) and Jäger et al. (2001). These concepts can be immediately generalized to the 3-D case by performing the same hypothetical experiments as in 2-D. Some snapshots of the emerging wavefronts are displayed in Figure 1 for a model consisting of three homogeneous layers. Obviously, the curvatures can no longer be described by scalars but take the form of 2×2 matrices. The propagation direction can now be described by a unit vector with three components or, more convenient, by its projection onto the acquisition surface. Considering the symmetry of the curvature matrices, we come up with a set of eight wavefield attributes. Nevertheless, the hyperbolic CRS stacking operator formally remains the same as for

[1] In 3-D, the stacking velocity in general depends on the azimuth.

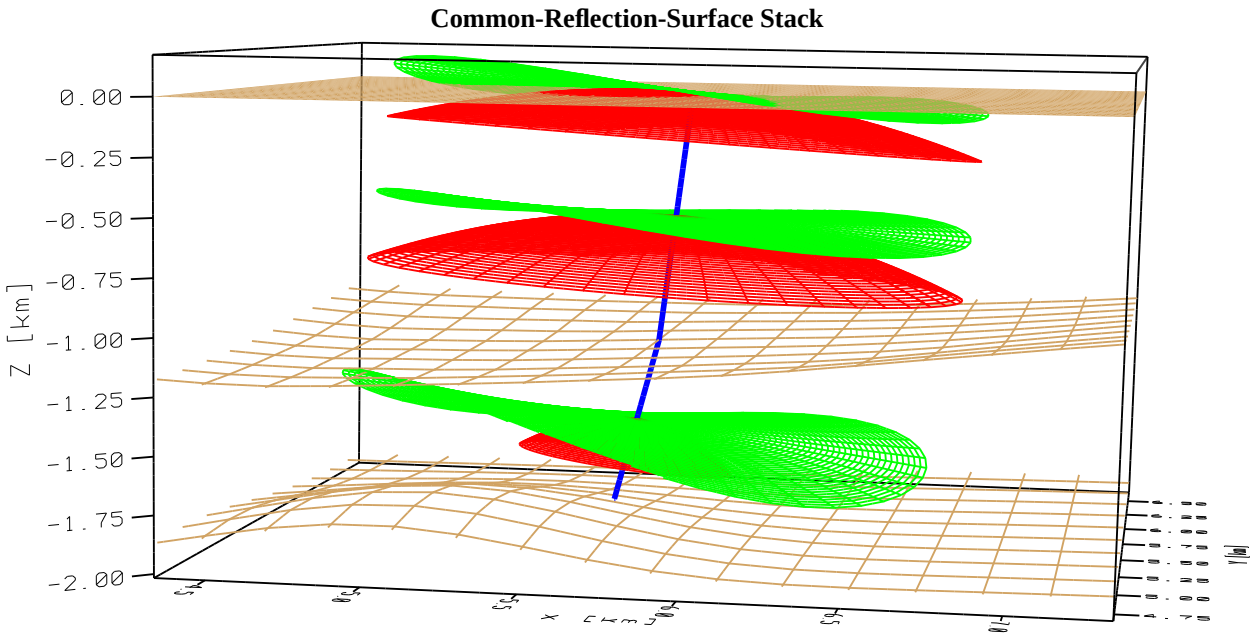

Fig. 1: Hypothetical experiments yielding the wavefield attributes for the 3-D CRS stack for ZO. The normal ray (bold blue line) connects the normal incidence point on the second interface (brown grid) with the acquisition surface (brown plane). The red and green surfaces represent the emerging NIP and normal wavefronts, respectively, for three different instances of time.

the 2-D case:

$$t^2 = \left(t_0 + \frac{2}{v}\, \mathbf{w_z} \circ \mathbf{m} \right)^2 + \frac{2t_0}{v}\, \mathbf{m^T}\, \hat{\mathbf{A}}\, \mathbf{m} + \frac{2t_0}{v}\, \mathbf{h^T}\, \hat{\mathbf{B}}\, \mathbf{h}\,. \tag{1}$$

The matrices $\hat{\mathbf{A}}$ and $\hat{\mathbf{B}}$ depend on the curvatures of the normal and the NIP wave, respectively, and the projected propagation direction $\mathbf{w_z}$. $\mathbf{m}$ and $\mathbf{h}$ denote the relative midpoint displacement vector and the half offset vector, respectively. As in the 2-D case, t_0 is the traveltime to be simulated, and v denotes the near-surface velocity.

To fit the optimum stacking operator to an actual reflection event, a global optimization in an eight-dimensional parameter domain would be required. However, the computational effort for such an optimization is unacceptable. Similar to the implementation strategy for 2-D (see, e. g., Jäger et al., 2001), the eight-parameter problem can be split into separate optimizations with less parameters. Among other strategies, one way to solve this problem is to decompose it into a set of 2-D problems: in case of sufficient azimuthal coverage in the pre-stack data, the CRS stack for 2-D can be applied independently for lines with three different azimuths. The 3×3 wavefield attributes from this approach can be combined to the eight wavefield attributes in Equation (1).

In case of poor azimuthal coverage, the curvature of the NIP wavefront cannot be fully determined because of the lack of information in the acquired data: if, e. g., only one small azimuth range is covered, the five-dimensional $(t, \mathbf{m}, \mathbf{h})$ data domain is virtually four-dimensional as all half-offset vectors $\mathbf{h}$ are almost parallel. An additional assumption, e. g., spherical NIP wavefronts, is required for a complete description of the CRS stacking operator.

2-D finite-offset simulation

For ZO simulation, we considered rays with coincident up-going and down-going ray branches. However, in case of finite offset (FO) and/or converted waves, the two ray branches no longer coincide. However, the described two hypothetical experiments with NIP and normal wavefronts provide only information about the reflector segment and the propagation along the normal ray. Thus, different hypothetical experiments are required to associate the reflector segment's properties with wavefield attributes in the time domain—these experiments have to provide information about *both* ray branches of the FO ray.

Appropriate hypothetical experiments for the FO case were introduced by Zhang et al. (2000). The first experiment is the so-called common-shot (CS) experiment[2] for which a point source is placed in the shot point of the considered FO ray. The CS wavefront propagates along the down-going ray branch, is reflected at the reflector segment, and propagates back to the acquisition surface along the up-going ray branch. This experiment defines three wavefield attributes, namely the curvature of the wavefront K_1 emerging at the receiver and the propagation direction along the FO ray at the source and the receiver, respectively. The propagation directions can be described by the angles between the FO ray branches and the acquisition surface normal.

[2] "Common" refers to the paraxial rays in the vicinity of the central FO ray.

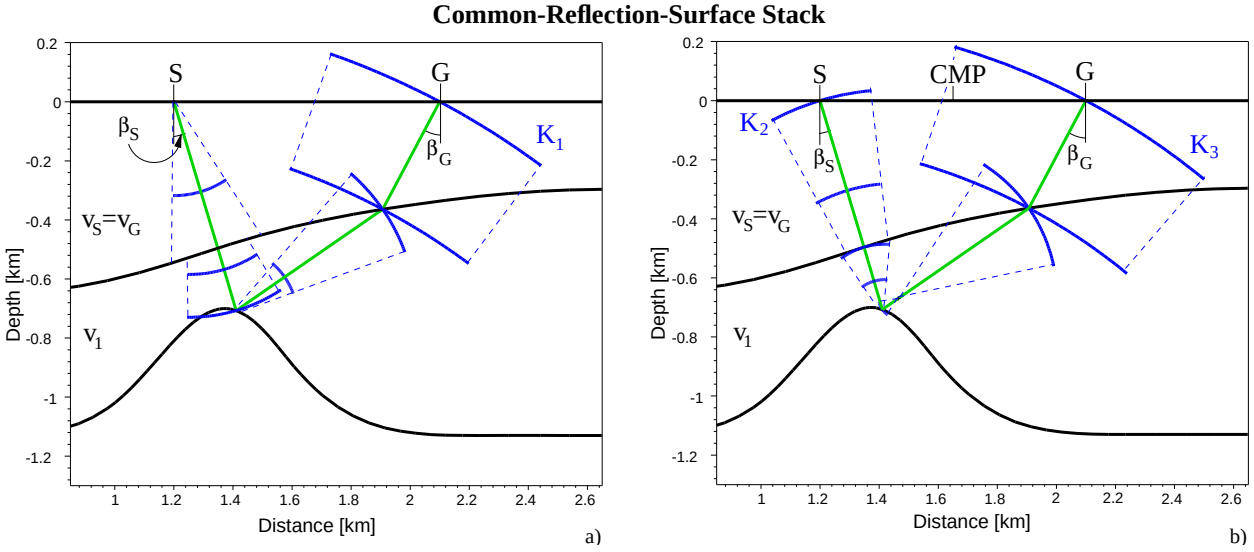

Fig. 2: Hypothetical experiments yielding the wavefield attributes for the 2-D CRS stack for FO. The FO ray (bold green line) connects the reflection point on the second interface with the acquisition surface. The blue lines represent the a) CS and b) CMP wavefronts, respectively, for different instances of time. The propagation directions along the FO ray are given by β_S and β_G at the shot and the receiver, respectively. K_1, K_2, and K_3 denote the curvatures of the wavefronts at the indicated locations.

The CS experiment is depicted in Figure 2a for a model consisting of three homogeneous layers.

The second experiment, the so-called common-midpoint (CMP) experiment[2], is more difficult to explain: the initial curvature of the wavefront starting at the source is now no longer zero (as in the CS experiment) but takes a finite value K_2. This wavefront also propagates along the FO ray via the reflecting interface to the receiver and emerges with the curvature K_3 (see Figure 2b). The propagation direction along the FO ray is the same as for the CS experiment. Thus, we come up with a set of five wavefield attributes for the FO case. For offset zero, the number of attributes again reduces to three: the two angles, β_S and β_G, coincide and the three curvatures, K_1, K_2, and K_3, can be expressed in terms of the two curvatures related to the normal and NIP wave experiment introduced for the ZO case.

The hyperbolic approximation of the kinematic reflection response of the reflector segment for FO in terms of the five wavefield attributes is given in Equation (2). (t_0, x_0, h_0) defines the FO sample to be simulated, whereas x_m and h denote the midpoint and half-offset coordinates of the contributing traces. The near-surface velocities at shot and receiver are given by v_S and v_G, respectively. Similar to the ZO case, the search for these attributes can be performed in separate steps and specific gathers. In each gather, the CRS stacking operator is a two-parameter hyperbola. We determine two parameters in the CMP gather, two in the common-offset (CO) gather, and the last one in the CS gather (the second CS parameter is not independent).

The presented approach for the simulation of 2-D FO sections can be generalized to the 3-D case by performing the same hypothetical experiments. As for the ZO case, the propagation directions are then given by two component vectors, whereas the curvatures are symmetric 2×2 matrices. This yields a total of 13 wavefield attributes. The development of efficient strategies to determine these attributes remains as a future research topic.

As already indicated above, the CRS stack for FO simulation can also handle converted waves. In this case, the near-surface velocities at shot and receiver, v_S and v_G, refer to the respective wave types.

Applications of the attributes

The CRS stacking operator approximates the kinematic *reflection* response of a curved reflector segment. By simply setting the curvature of the normal wave equal to the curvature of the NIP wave for the ZO case, we obtain a second-order approximation of the kinematic *diffraction* response of the associated point in depth. The apex of this response readily provides the image location for time migration. Placing the stack result into this apex location yields a time migrated image without requiring an explicit velocity model, see Mann et al. (2000).

The traveltime difference Δt between the approximated reflection and diffraction responses serves to estimate the projected first Fresnel zone by means of the condition $\Delta t \leq 1/2f$, with f denoting the dominant wavelet frequency (Hubral et al., 1993). The projected Fresnel zone allows to perform a subsequent parsimonious migration, i. e., a migration restricted to the actual region of tangency between the migration operator and the reflection event. This speeds up the migration process and provides an optimum signal-to-noise ratio in the migrated image.

The CRS stack method uses much more traces to determine the wavefield attributes than, e. g., NMO/DMO/stack. Thus, the attributes are more stable and reliable than the stacking velocity obtained from conventional velocity analysis. The stacking velocity can be expressed in terms of the CRS attributes. With the known incidence and emergence directions[3] of the central ray,

[3]Both directions coincide in the ZO case.

$$
\begin{aligned}
t^2 = & \left[t_0 + \left(\frac{\sin\beta_G}{v_G} + \frac{\sin\beta_S}{v_S} \right) (x_m - x_0) + \left(\frac{\sin\beta_G}{v_G} - \frac{\sin\beta_S}{v_S} \right) (h - h_0) \right]^2 \\
& + 2t_0 \left[(x_m - x_0) \left(K_3 \frac{\cos^2\beta_G}{v_G} + K_2 \frac{\cos^2\beta_S}{v_S} \right) (h - h_0) \right. \\
& + \frac{1}{2} (x_m - x_0) \left((4K_1 - 3K_3) \frac{\cos^2\beta_G}{v_G} - K_2 \frac{\cos^2\beta_S}{v_S} \right) (x_m - x_0) \\
& \left. + \frac{1}{2} (h - h_0) \left(K_3 \frac{\cos^2\beta_G}{v_G} - K_2 \frac{\cos^2\beta_S}{v_S} \right) (h - h_0) \right] .
\end{aligned}
\tag{2}
$$

this approach also provides the RMS velocity that is suited for subsequent processes like a Dix-type inversion, etc.

As shown by Newman (1973), kinematic wavefront properties also provide information about dynamic characteristics of the wavefield. Generalizing his approach the kinematic CRS attributes can be related to the geometrical spreading factor along the central ray. The geometrical spreading factor serves as a natural gain function for the simulated ZO or FO section and for true-amplitude analysis.

Last but not least, we would like to indicate that the CRS attributes are also suited to construct a layered model with constant velocity in each layer. However, this layer-stripping approach requires the picking of key events in the CRS stacked section and their associated wavefield attributes. Details can be found in Majer (2000).

Conclusions

The CRS stack method, originally introduced for the simulation of 2-D ZO sections, has been generalized for the simulation of 3-D ZO sections as well as 2-D FO sections. For an efficient implementation, the 3-D ZO CRS stack can, e. g., be decomposed to separate 2-D ZO problems. An implementation strategy for the 2-D FO CRS stack was discussed. Its generalization to 3-D remains as subject for future research.

The data-driven simulation of FO sections opens up new possibilities for various applications. As an example, the FO CRS stack can be used to simulate a set of FO sections with high signal-to-noise ratio which are well suited as input for tomographic methods.

Several useful seismic applications of the wavefield attributes have been discussed for the 2-D ZO case. Analogous expressions can be derived for the more general 3-D and/or FO approaches.

Acknowledgments

We would like to thank the sponsors of the Wave Inversion Technology (WIT) Consortium for their support.

References

Hubral, P., Schleicher, J., Tygel, M., and Hanitzsch, C., 1993, Determination of Fresnel zones from traveltime measurements: Geophysics, **58**, no. 5, 703–712.

Jäger, R., Mann, J., Höcht, G., and Hubral, P., 2001, Common-reflection-surface stack: Image and attributes: Geophysics, **66**, no. 1, 97–109.

Majer, P., 2000, Inversion of seismic parameters: Determination of the 2-D iso-velocity layer model: Master's thesis, Universität Karlsruhe.

Mann, J., Jäger, R., Müller, T., Höcht, G., and Hubral, P., 1999, Common-reflection-surface stack - a real data example: J. Appl. Geoph., **42**, no. 3,4, 301–318.

Mann, J., Hubral, P., Traub, B., Gerst, A., and Meyer, H., 2000, Macro-Model Independent Approximative Prestack Time Migration: 62th Mtg., Eur. Assn. Geosci. Eng., Extended Abstracts.

Mann, J., 2001, Common-Reflection-Surface Stack and conflicting dips: 63th Mtg., Eur. Assn. Geosci. Eng., Extended Abstracts.

Müller, T., Jäger, R., and Höcht, G., 1998, Common reflection surface stacking method - imaging with an unknown velocity model: 68th Annual Internat. Mtg., Soc. Expl. Geophys., Expanded Abstracts, 1764–1767.

Müller, T., 1998, Common Reflection Surface Stack versus NMO/STACK and NMO/DMO/STACK: 60th Annual Internat. Mtg., Eur. Assn. Geosci. Eng., Extended Abstracts, Session 1-20.

Newman, P., 1973, Divergence effects in a layered earth: Geophysics, **38**, no. 3, 481–488.

Zhang, Y., Bergler, S., Tygel, M., and Hubral, P., 2000, Model-independent traveltime attributes for 2-D, finite-offset multicoverage reflections: Accepted by Pure Appl. Geophys.